

Hollow MoS₃ Nanospheres as Electrode Material for “Water-in-Salt” Li-Ion Batteries

Quan, Ting; Xu, Yaolin; Tovar, Michael; Goubard-Bretesché, Nicolas; Li, Zhaolong; Kochovski, Zdravko; Kirmse, Holm; Skrodzky, Kai; Wagemaker, Marnix; More Authors

DOI

[10.1002/batt.202000042](https://doi.org/10.1002/batt.202000042)

Publication date

2020

Document Version

Final published version

Published in

Batteries and Supercaps

Citation (APA)

Quan, T., Xu, Y., Tovar, M., Goubard-Bretesché, N., Li, Z., Kochovski, Z., Kirmse, H., Skrodzky, K., Wagemaker, M., & More Authors (2020). Hollow MoS₃ Nanospheres as Electrode Material for “Water-in-Salt” Li-Ion Batteries. *Batteries and Supercaps*, 3(8), 747-756. <https://doi.org/10.1002/batt.202000042>

Important note

To cite this publication, please use the final published version (if applicable).
Please check the document version above.

Copyright

Other than for strictly personal use, it is not permitted to download, forward or distribute the text or part of it, without the consent of the author(s) and/or copyright holder(s), unless the work is under an open content license such as Creative Commons.

Takedown policy

Please contact us and provide details if you believe this document breaches copyrights.
We will remove access to the work immediately and investigate your claim.

Hollow MoS₃ Nanospheres as Electrode Material for “Water-in-Salt” Li-Ion Batteries

Ting Quan,^[a] Yaolin Xu,^{*[a]} Michael Tovar,^[b] Nicolas Goubard-Bretesché,^[c] Zhaolong Li,^[d] Zdravko Kochovski,^[a] Holm Kirmse,^[e] Kai Skrodczky,^[f] Shilin Mei,^[a] Hongtao Yu,^[a] Daniel Abou-Ras,^[b] Marnix Wagemaker,^[d] and Yan Lu^{*[a, g]}

The use of “water-in-salt” electrolyte (WISE) (i.e., a highly concentrated aqueous solution) in rechargeable batteries has received increasing attention due to the significantly expanded electrochemical window compared to the limited voltage of conventional aqueous electrolytes. It enables the use of more positive/negative electrode material couples in aqueous batteries, resulting in an enhanced output voltage. However, one of the challenges is to identify promising anode materials for the “water-in-salt” Li-ion batteries (WIS-LIBs). Herein we for the first time demonstrate that MoS₃, an amorphous chain-like structured transitional metal trichalcogenide, is promising as anode in the WIS-LIBs. In this work, hollow MoS₃ nanospheres were synthesized via a scalable room-temperature acid precipitation method. When applied in WIS-LIBs, the prepared MoS₃

achieved a high specific capacity of 127 mAh/g at the current density of 0.1 A/g and good stability over 1000 cycles. During operation, MoS₃ underwent irreversible conversion to Li₂MoO₄ (with H₂S and H₂ evolution) during the initial Li ion uptake, and was then converted gradually to a more stable and reversible Li_xMoO_y (2 ≤ y ≤ 4) phase along cycling. Amorphous Li-deficient Li_{x-m}MoO_y/MoO_z was formed upon delithiation. Nevertheless, MoS₃ outperformed MoO₃ in WIS-LIBs, which could be accredited to its initial one-dimensional molecular structure and the amorphous nature of the delithiated product facilitating charge transport. These results demonstrated a novel routine for synthesizing metal sulfides with hollow structures using a template-based method and push forward the development of metal sulfides for aqueous energy storage applications.

[a] T. Quan, Dr. Y. Xu, Dr. Z. Kochovski, Dr. S. Mei, Dr. H. Yu, Prof. Y. Lu
Institute for Electrochemical Energy Storage
Helmholtz-Zentrum Berlin für Materialien und Energie
Hahn-Meitner-Platz 1, 14109 Berlin, Germany
E-mail: yaolin.xu@helmholtz-berlin.de
yan.lu@helmholtz-berlin.de

[b] Dr. M. Tovar, Dr. D. Abou-Ras
Department Structure and Dynamics of Energy materials
Helmholtz-Zentrum Berlin für Materialien und Energie
Hahn-Meitner-Platz 1, 14109 Berlin, Germany

[c] Dr. N. Goubard-Bretesché
Département de Chimie
Université Du Québec à Montréal (UQAM)
Case Postale 8888, Succursale Centre-Ville,
Montréal, Québec, H3C 3P8, Canada

[d] Dr. Z. Li, Dr. M. Wagemaker
Storage of Electrochemical Energy (SEE)
Department of Radiation Science and Technology,
Faculty of Applied Science
Delft University of Technology
Mekelweg 15, 2629 JB Delft, The Netherlands

[e] Dr. H. Kirmse
Institut für Physik
Humboldt-Universität zu Berlin
Newtonstraße 15, 12489 Berlin, Germany

[f] K. Skrodczky
Institut für Chemie
Humboldt-Universität zu Berlin
Brook-Taylor-Str. 2, 12489 Berlin, Germany

[g] Prof. Y. Lu
Institute of Chemistry
University of Potsdam
14467 Potsdam, Germany

© 2020 The Authors. Published by Wiley-VCH Verlag GmbH & Co. KGaA. This is an open access article under the terms of the Creative Commons Attribution License, which permits use, distribution and reproduction in any medium, provided the original work is properly cited. Supporting information for this article is available on the WWW under <https://doi.org/10.1002/batt.202000042>

1. Introduction

Among all the energy storage systems for portable electronic and electrical vehicles, rechargeable lithium ion batteries (LIBs) are dominating the market due to their high energy density, long lifetime, and high energy efficiency.^[1] However, the safety issues related to the flammable, thermally unstable and electrode-/chemically reactive liquid organic electrolytes limit their adoption in many applications, e.g., large-scale grid electricity storage.^[2] Aqueous electrolytes are an attractive alternative, which allows to manufacture batteries in the natural environment and systems,^[3] but their electrochemical stability window is narrow due to water splitting at > 1.23 V, limiting their energy and power density. Particularly, at low potential values (typically 2.2 to 3.0 V vs. Li⁺/Li depending on the pH value), the hydrogen evolution reaction (HER) occurs, which severely deteriorates the electrode structure and also presents safety challenges.^[4]

Recently, L.M. Suo et al.^[5] reported that a significantly expanded voltage window up to ~3 V can be achieved for a super-concentrated aqueous electrolyte, namely a “water-in-salt” electrolyte (WISE). The WISE extends the operational voltage, enables more choices of electrode materials, and suppresses the safety issues (e.g., gas-evolution) of conventional aqueous batteries.^[6] The expanded potential window is a consequence of the very small molecular ratio of water-to-salt in the electrolyte, which leads to a low fraction of free water molecules and increases the oxidative stability of water molecules and electrolyte anions.^[7] In addition, the salt-rich interface in these electrolytes serves as an electron barrier

preventing the reduction of water while allowing Li^+ migration.^[8] Such a wide voltage window provides unprecedented flexibility in selecting the anode-cathode couples, enabling the utilization of many electrode materials that are unsuitable in traditional aqueous electrolytes.^[9] As a result, WISEs have attracted intensive research interest.^[10]

The electrode material is one of the key factors that influence the electrochemical performance of LIBs.^[11] Transition metal sulfides (TMSs) are promising due to their high specific capacity and structure merits.^[12] Among TMSs, for LIBs, MoS_2 has drawn special attention due to the facile Li ion intercalation in the layered structure.^[12c,13] However, it suffers from severe volume change during charge/discharge resulting in limited cycling stability. In addition, MoS_2 based nanomaterials are usually prepared through a hydrothermal method,^[14] which is costly and energy intensive. As an alternative, MoS_3 has recently been widely explored,^[15] which was introduced as an electrode material in LIBs in 1979^[16] but was rarely studied in LIBs in the following 30 years. MoS_3 exhibits superior properties for LIBs compared to MoS_2 . Firstly, MoS_3 consists of chains of Mo atoms bridged by two ligands, one sulfide (S^{2-}) and one disulfide (S_2^{2-}).^[17] This one-dimensional chain structure has more open sites toward Li ion storage during the electrochemical reaction, and thus provides a higher specific capacity. Secondly, it is amorphous and has lower activation energy barriers for the structural rearrangement during Li-ion uptake.^[18] Thirdly, it has a higher electrical conductivity than MoS_2 (band gap of <1.5 eV for MoS_3 vs. 1.8 eV for MoS_2 ^[19]), which improves the electron transfer efficiency in LIBs. Moreover, MoS_3 can be facilely synthesized from MoS_4^{2-} at room temperature under ambient pressure.^[20] All these merits make MoS_3 an attractive candidate for battery applications. For example, Zhou *et al.* studied ultra-small MoS_3 loaded graphene oxide nanocomposites as anode material for LIBs with 1 M LiPF_6 in a mixed solvent of ethylene carbonate (EC) and dimethyl carbonate (DMC) (1:1 v/v) as electrolyte, which achieved a reversible specific capacity of 685 mAh/g after 1000 cycles at a high current density of 2 A/g.^[21] Chang *et al.* hybridized reduced graphene oxides with MoS_3 nanosheets and showed a capacity of about 900 mAh/g at a rate of 5 C for 2500 cycles without capacity fading in LIBs with 1 M LiPF_6 in ethylene carbonate: diethyl carbonate (1:1, v/v %) as electrolyte.^[15a]

Despite these research efforts, the working mechanism for Li-ion storage in MoS_3 in organic electrolytes remains unclear and controversial, largely hindering its development. Chang presented that, during the initial cycles, amorphous MoS_3 is converted to crystalline MoS_2 and Li_2S .^[15a] X. Li reported that the lithiation of MoS_3 involves in the generation of amorphous Li_xMoS_3 in Li-ion batteries.^[22] Moreover, MoS_3 suffers from severe volume change upon Li-ion absorption, which, upon repetitive dis-/charge, will lead to material pulverization and capacity decay.^[23] Furthermore, MoS_3 is stable in aqueous solutions, but remains unexplored in aqueous electrolytes based LIBs, which may be limited by the low potential of Li ion uptake in MoS_3 , about 2.0 V vs. Li/Li^+ ,^[18] at which HER happens in conventional aqueous electrolytes.

In the present work, we report MoS_3 hollow nanospheres as anode material in WISE-based LIBs (WISE-LIBs), using a bistrifluoromethanesulfonimide lithium salt (LiTFSI) based WISE that has a low potential limit of 1.9 V vs. Li/Li^+ .^[5] As the lithiation potential of MoS_3 is close to the lower potential limit of the WISE, it enables the full utilization of the offered electrochemical stability window of the WISE, and maximizes the working voltage and thus the energy and power density, when paired with an appropriate cathode material (e.g., LiMn_2O_4 in this work). Hollow MoS_3 nanospheres were facilely synthesized using spherical polyelectrolyte brushes (SPB) as carriers and templates at room temperature. The SPB nanospheres are suspended in water and soluble in tetrahydrofuran (THF),^[24] making the preparation simple and scalable. The hollow nanostructure accommodates the volume change effectively upon repeated uptake/release of Li ions and enhances the cycle life of electrode materials.^[25] This work also studies the reaction mechanisms of MoS_3 in the WISE-LIBs, providing insights in the direction towards its future improvement as well as the development of TMSs for aqueous LIBs.

2. Results and Discussion

In our previous work, SPB has been demonstrated as a promising nanoreactor for immobilizing metal nanoparticles due to the strong localization of their counterions on the surface.^[26] Inspired by that, the cationic SPB particles with chains of PAEMH grafted on PS cores were used as a template and immobilizer of anionic MoS_4^{2-} to synthesize hollow MoS_3 particles in this work. Specifically, as illustrated in Figure 1, MoS_4^{2-} , the precursor of MoS_3 , was adsorbed on the surface layer of SPB chains due to the electrostatic adsorption. Upon acid addition, MoS_3 precipitated homogeneously onto the surface of SPB particles following the reaction: $\text{MoS}_4^{2-} + 2\text{H}^+ = \text{MoS}_3\downarrow + \text{H}_2\text{S}\uparrow$.^[17] The hollow structure was obtained after removing the SPB template with THF. The cryo-TEM image of SPB- MoS_3 (Figure 2(a)) demonstrates that, before removal of the SPB template, the MoS_3 nanoparticles are immobilized within the brushes and no free MoS_3 particles are observed. The as-synthesized MoS_3 after the removing of SPB templates in Figure 2(b) and Figure S1(c) shows a spherical morphology with the diameter of about 100 nm. The hollow structure of the MoS_3 nanospheres is evidenced, judging from the significant contrast between the shell and the inner part. The thickness of the MoS_3 shell is about 5 nm, according to the high-resolution TEM images in Figure 2(c). From the STEM-based HAADF imaging and EDS elemental mapping, it can be seen that Mo and S elements are located within the shell of the particle (Figure 2(d)–2(f)).

The as-synthesized hollow MoS_3 nanospheres present a highly colloidally stable system. As shown in Figure 3(a), the suspension of hollow MoS_3 nanospheres in water remains stable after standing over 24 h at room temperature. XRD, Raman spectroscopy and XPS were applied to identify the chemical composition of the as-synthesized hollow nanospheres. The synthesized MoS_3 appears to be amorphous,

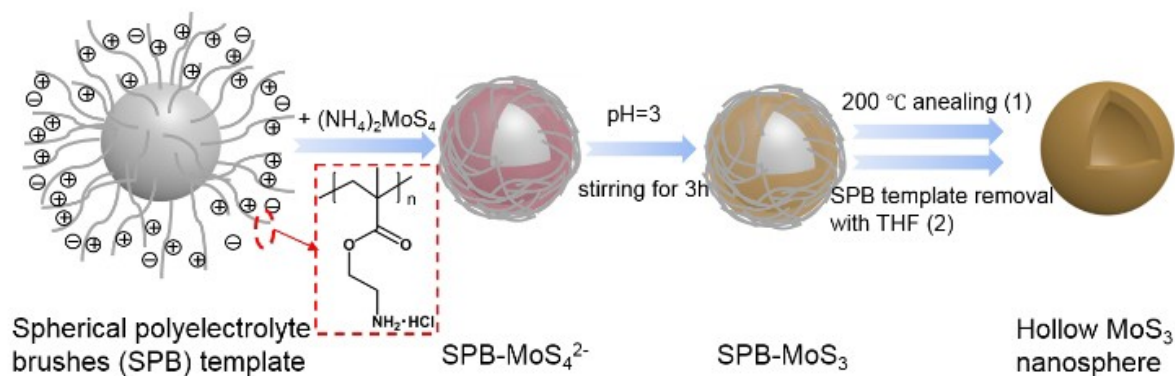


Figure 1. Schematic representation for the synthesis of hollow MoS_3 nanospheres.

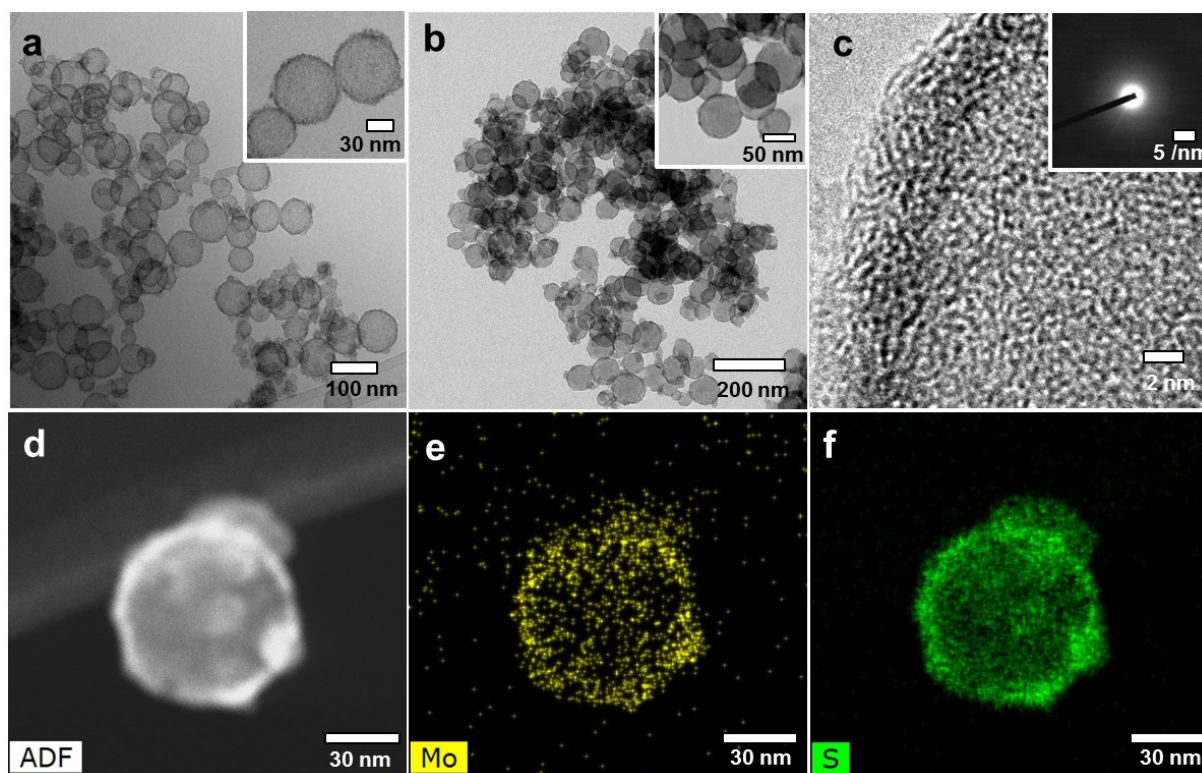


Figure 2. Electron microscopic characterization of hollow MoS_3 nanospheres. a) Cryo-TEM images of SPB- MoS_3 nanospheres before annealing, b-c) TEM images of hollow MoS_3 nanospheres, d) STEM-HAADF image of a hollow MoS_3 nanosphere, and e and f) its corresponding EDS elemental mappings.

which is evidenced by high-resolution TEM images and the diffuse halo rings in the selected area electron diffraction (SAED) pattern in Figure 2(c). This is in good agreement with the XRD pattern (Figure 3(b)), which shows a featureless spectrum except for a broad and diffuse hump at 14° from amorphous MoS_3 .^[18] The Raman spectrum (Figure 3(c)) shows distinctive peaks at 242, 280, 338, 378, 465 cm^{-1} corresponding to the various Mo–S stretches in MoS_3 .^[27] Furthermore, the $\text{Mo}3d_{3/2}$ and $\text{Mo}3d_{5/2}$ doublet binding energies are located at 232.5 eV and 229.3 eV in the Mo 3d XPS spectra (Figure 3(d)), respectively, corresponding to the Mo^{4+} in MoS_3 .^[28] The S 2p spectrum (Figure 3(e)) shows a broad envelope consisting of two doublets which are assigned to the bridging S_2^{2-} and/or

apical S^{2-} ligands and terminal S_2^{2-} and/or S^{2-} . The lower binding energy peak of the doublet is assigned to terminal disulfide and/or sulfide ligands, while the higher is assigned to bridging disulfide and/or apical sulfide ligands.^[23] Notably, these results are well in line with the previous reports on MoS_3 . Meanwhile, the SEM-based EDS on the as-synthesized product in Figure S1(d) reveals that the atom ratio between Mo and S amounts is about 1:3, which also represents its chemical content in the form of MoS_3 . A BET specific surface area of 87 m^2/g has been determined for the hollow MoS_3 nanospheres (Figure 3(f)), which is higher than the reported MoS_3 nanomaterials.^[29] From the Barrett-Joyner-Halenda (BJH) pore size distribution curve in the inset of Figure 3(f), a peak with

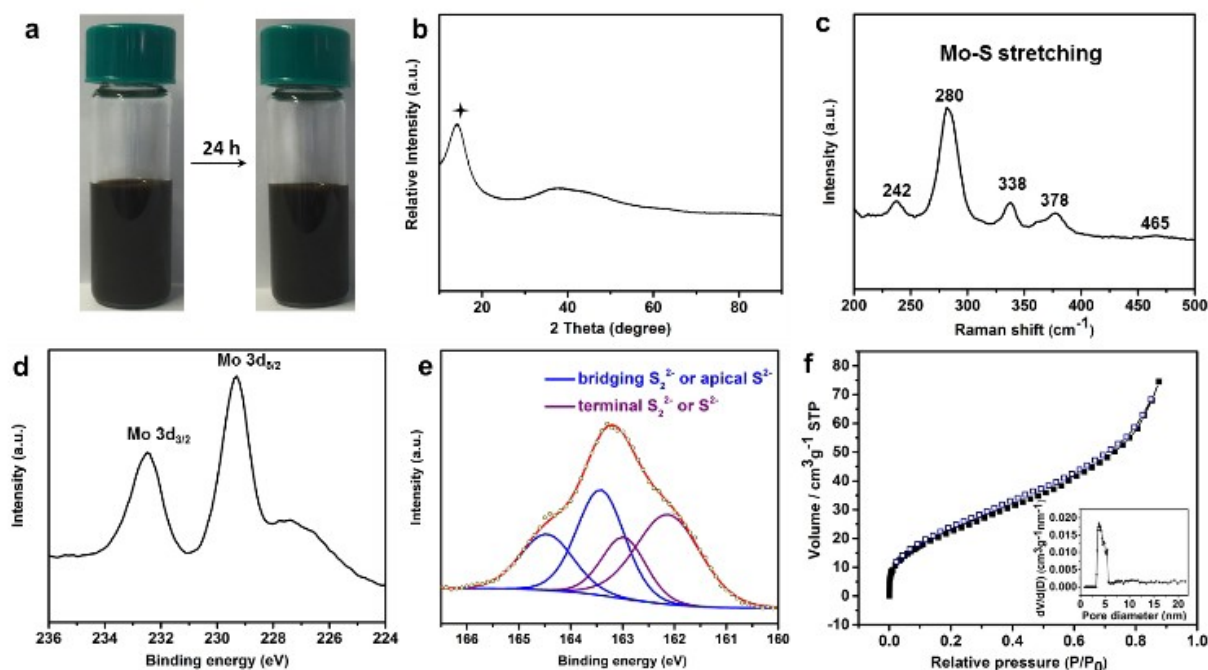


Figure 3. Spectroscopic characterization of hollow MoS_3 nanospheres. a) Photographs of the hollow MoS_3 nanospheres dispersion in water, b) XRD pattern, c) Raman spectrum, d) Mo 3d XPS spectrum, e) S 2p XPS spectrum and f) Nitrogen adsorption/desorption isotherms. The inset in panel f) shows the pore size distribution obtained using the BJH method.

pore size of about 5 nm is found, indicating its mesoporous structure. The mesoporous structure and high specific surface area facilitate the electrolyte infiltration and Li ions uptake when applied in LIBs.

Note that the MoS_3 hollow spheres demonstrate a high specific surface area facilitating ion diffusion, and exhibit a high dispersity and colloidal stability in water as indicated above, making it particularly suitable for aqueous battery systems. The hollow MoS_3 nanospheres were firstly measured in a three-electrode configuration to study the potential window of the material in WISE. In this system, Pt wire and Ag/AgCl were used as the counter and reference electrode, respectively. As shown in Figure S2, a stability window of ≈ 3.1 V was achieved, with the cathodic limit at -1.2 V (vs. Ag/AgCl), below which significant HER occurs due to the splitting of water in the electrolyte. The peak at around -0.7 V (vs. Ag/AgCl) is related to the phase transformation of MoS_3 , which is also inevitably accompanied with a certain amount of H_2 evolution for charge balance, during the cathodic scan. In this work, the electrochemical properties of MoS_3 hollow spheres were evaluated in WISE-based $\text{LiMn}_2\text{O}_4/\text{MoS}_3$ coin cells, in which MoS_3 and LiMn_2O_4 were used as the anode and cathode material, respectively, and a 21 m LiTFSI aqueous solution based WISE was served as the working electrolyte. LiMn_2O_4 has demonstrated a high cycling stability in such electrolyte over 1000 cycles.^[5] Figure S3(a) demonstrates that a significant HER process occurs when the voltage is higher than 1.8 V in 1 m LiTFSI, while no obvious HER peaks can be observed up to 2 V when using the 21 m LiTFSI, indicating the suppressed oxygen evolution and higher electrochemical stability of aqueous Li-ion

batteries when a WISE electrolyte is used. This can be attributed to the low fraction of free water molecules^[8a] and the formation of a solid electrolyte interphase (SEI).^[5]

The CV curve at the scan rate of 1 mV/s in Figure 4(a) shows one broad but distinct redox peak couple of lithiation/delithiation after the initial two cycles. In the initial cycles, the cathodic scan (i.e. battery charging) profile transforms from a relatively featureless curve at the first cycle to a broad peak at about 1.8 V from the fifth cycle, implying an irreversible phase transformation of MoS_3 during its lithiation at the initial cycles. The cathodic scan profile remains rather stable after 5 cycles, indicating the stabilization and reversibility of electrode materials after the initial transformation. Meanwhile, an anodic peak can be observed around 1.5 V during battery discharging, corresponding to the release of Li-ions from the lithiated product of MoS_3 and their insertion into the cathode material. At different scan rates, the CV curves in Figure 4(b) keep their typical shape while the peaks shift gradually to a higher voltage during charge and a lower one during discharge when increasing the scan rate, indicating a diffusion-controlled battery-type energy storage. After log-log calculation of the anodic peak (marked as #), a linear relationship can be observed between the scan rate and peak current density (inset of Figure 4(b)). The kinetic factor which determines the reaction here can be identified by the parameter b with the equation $i = av^b$ (i is the peak current density, and v is the scan rate), where $b=1$ represents a surface-controlled reaction, corresponding to capacitive behavior, and $b=0.5$ represents a diffusion-controlled reaction, corresponding to a battery-type behavior.^[30] The b value for the anodic peak in this study is 0.74, indicating

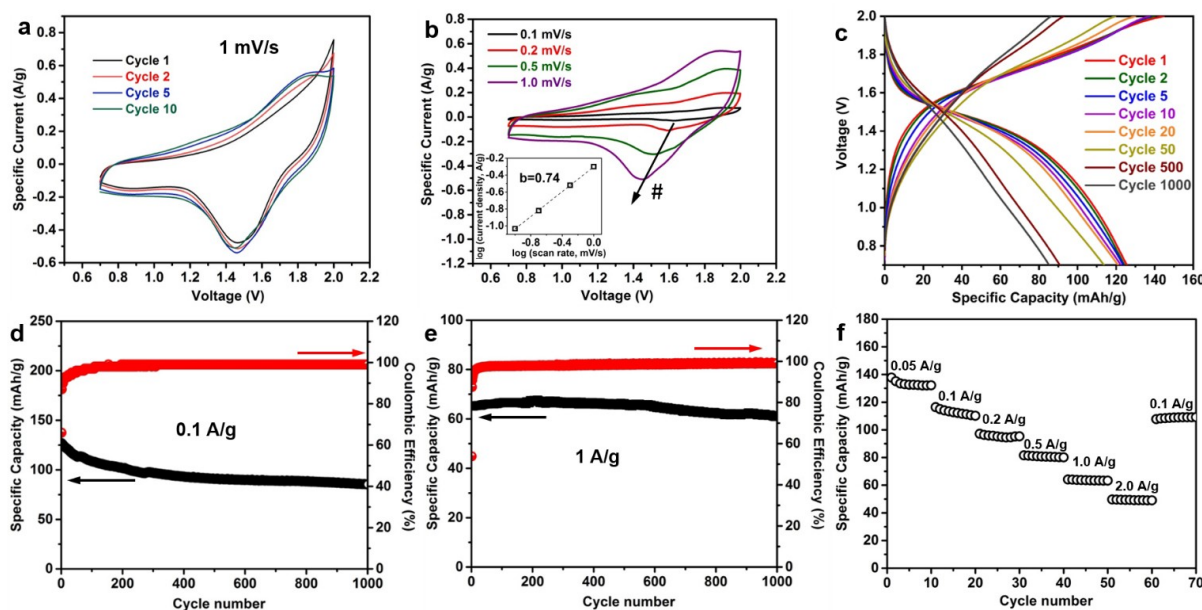


Figure 4. Electrochemical performance of the WISE-based $\text{LiMn}_2\text{O}_4/\text{MoS}_3$ coin cells. a) Cyclic voltammetry curves at initial cycles at 1 mV/s and b) at different scanning rates (the inset shows the log-log fitting by equation $i = av^b$, where i is the peak current density, and v is the scan rate), c) galvanostatic charge-discharge profiles at different cycles at 0.1 A/g, d) the cycle life and Coulombic efficiency at 0.1 A/g, e) the cycle life and Coulombic efficiency at 1 A/g and f) Rate capability.

contribution from both capacitive and battery-type charge storage: the high specific surface area arising from hollow nanostructure facilitates a surface-controlled Li-ion adsorption, while Li-ion storage in the bulk part of the active material behaves a diffusion-controlled reaction.

The galvanostatic dis-/charge curve in Figure 4(c) shows a sloping voltage plateau at ~ 1.7 V (mid-voltage) during charge and ~ 1.5 V during discharge, despite that it appears to be more sloped in the initial cycle. These observations, together with the differential capacity (dQ/dV) profile (Figure S3(b)) recalculated from the voltage profile, are in good agreement with the results of CV (Figure 4(a)). It supports that MoS_3 first undergoes irreversible conversion and then remains stable. The detailed reactions during cycling are elucidated and described in the latter part of this work.

The cycling stability of the full cell was evaluated at both low (0.1 A/g, Figure 4(d)) and high (1 A/g, Figure 4(e)) current densities for 1000 cycles. The specific capacity of MoS_3 amounts to 127 mAh/g at 0.1 A/g and 65.1 mAh/g at 1 A/g, respectively, for the first cycle. Excellent cycling stability is achieved with a capacity retention of 89 mAh/g and 61.2 mAh/g in 1000 cycles, corresponding to a capacity decay rate of 0.03% per cycle and 0.006% per cycle, at 0.1 A/g and at 1 A/g, respectively. Moreover, the initial Coulombic efficiency of the cell is merely 70% and 50% at 0.1 and 1 A/g, respectively, due to the irreversible phase transformation of MoS_3 and the formation of SEI.^[6b,32] The Coulombic efficiency increases to 90% after 2 cycles and approaches to $\geq 99\%$ afterwards at both current densities, revealing that the completion of phase transformation and formation of a stable and protective SEI has been achieved within as low as two cycles. This is also consistent with the CV and cycling voltage profiles.

In comparison, the galvanostatic charge-discharge profiles of bulk MoS_3 in Figure S5(b) appear to be more sloped with a much shorter voltage plateau. As a result, a lower specific capacity retention over long-term cycling is achieved compared to the hollow structured MoS_3 , specially, 89 mAh/g for hollow MoS_3 vs. 69 mAh/g for bulk MoS_3 in 1000 cycles at 0.1 A/g, though their initial capacities are rather comparable (127.3 and 116 mAh/g, respectively, for hollow and bulk MoS_3). Moreover, the Coulombic efficiency of the battery with bulk MoS_3 increases tardily and reaches 90% after as long as 30 cycles, which is also limited by the kinetics of Li ion diffusion. Such inferior performance originates from the sluggish Li ion diffusion in the bulk solid of MoS_3 and thus demonstrates the advantages of the hollow nanostructure in facilitating ion transport, especially at higher current rates. Despite that the high surface area of the hollow structure is unfavorable to aqueous systems causing H_2 evolution, it can facilitate the ionic transport, expedite the conversion of MoS_3 , and help to accommodate the changes in volume during lithiation and delithiation. In the present system, the H_2 evolution accompanied with the conversion of MoS_3 only takes place in the initial cycle. Eventually, it results in a better cycling stability than bulk materials with lower specific surface area.

To evaluate the rate capability, the cell was cycled at various current densities ranging from 0.05 A/g to 2 A/g (Figure 4(f)). At 2 A/g, MoS_3 demonstrates a capacity of 49.7 mAh/g, corresponding to 37% of the capacity at 0.05 A/g. Remarkably, a high capacity of 109 mAh/g can be recovered when the current density is reset to 0.1 A/g, implying that the relative lower capacity at a higher current rate is mainly limited by the poor kinetics of Li ion diffusion, not the degradation of electrode materials.

Table 1 lists the electrochemical performance of other reported WIS-LIBs in comparison with this work. The hollow MoS_3 nanospheres show a high specific capacity with the common used WIS electrolyte, which is comparable or superior to the reported electrode materials for WIS-LIBs, such as Mo_6S_8 ,^[5] TiO_2 ^[6b,31] and graphite.^[33] After long cycling, no matter at a low current density or a high current density, the cycling stability of hollow MoS_3 nanospheres is better than that of the reported materials even with improved electrolytes.

Encouraged by the outstanding coin cell performance, we further evaluated the performance of the $\text{LiMn}_2\text{O}_4/\text{MoS}_3$ based WIS-LIBs in pouch cells ($\sim 10\text{ cm}^2$) (Figure 5). The galvanostatic charge-discharge profiles of the pouch cell in Figure 5(b) are similar to those of coin cells, but the achieved capacity, 75 mAh/g at the initial cycle (Figure 5(c)), is lower, due to the lower compressive stack pressure in the pouch cell. Sufficient compressive stack pressure in LIBs is necessary to maintain intimate contact between battery components as well as to prevent layer delamination and deformation during operation.^[34] In addition, the differential capacity (dQ/dV) profiles (Figure S6) are similar to those of coin cells. From the 2nd cycle, the charging curves show a broad peak around 1.8 V rather than the unresolved one in the initial cycle, corresponding

to the irreversible transformation of MoS_3 during its initial lithiation, same as that in the coin cells.

The structural stability of hollow MoS_3 nanospheres is evidenced by post-mortem SEM characterization on cycled electrodes, as shown in Figure 6(a) and (b). The MoS_3 electrode keeps well-integrated after 400 cycles, and no evident structural deformation and crack could be observed in the cycled electrode. Meanwhile, the MoS_3 nanoparticles still remain their typical morphology and no structure collapse or aggregation can be found. Such structural integrity results in a low and stable electrical resistance, leading to the battery cycling stability. The excellent performance of the hollow MoS_3 nanospheres in the WIS-LIBs can be ascribed to the following features. (a) The hollow nanosphere structure and the one dimensional chained molecular structure of MoS_3 deliver many open sites toward Li^+ ion storage during the electrochemical reaction. (b) The hollow nanostructure is effective to relieve the structural strain from the repeated uptake/release of Li ions and thereby to prolong its cycle life. This is also supported by the electrochemical impedance spectroscopy (EIS) as shown in Figure S3(c) (d) and (e). The Nyquist plots have an intercept smaller than $15\ \Omega$ at the high frequency region related to the electronic resistance (R_b) of the electrode, followed by a

Table 1. Summary of the present work and recently reported materials in WIS-LIBs. The capacity values are presented in per mass of active material.

Cathode	Anode	Electrolyte	Average operating voltage [V]	Specific capacity of the anode material [mAh/g] and the applied current density ^[a]	Stability	Ref.
LiMn_2O_4	Mo_6S_8	LiTFSI (21 m)	1.4	141 (at 0.019 A/g)	78% after 100 cycles	[5]
LiFePO_4	Mo_6S_8	LiTFSI (21 m)	0.9	≈ 100 (at 0.13 A/g)	60% after 1000 cycles	[31]
LiMn_2O_4	C/ TiO_2	LiTFSI (21 m)	1.65	144 (at 0.075 A/g)	78% after 1000 cycles	[6b]
$\text{Li}_{0.5}\text{Mn}_{1.5}\text{O}_4$	$\text{Li}_4\text{Ti}_5\text{O}_{12}$	Li(TFSI) _{0.7} (BETI) _{0.3} ·2H ₂ O	3.1	≈ 120 (at 1 A/g)	63% after 100 cycles	[7a]
LiCoO_2	$\text{Li}_4\text{Ti}_5\text{O}_{12}$		2.4	≈ 120 (at 1.37 A/g)	75% after 200 cycles	
LiCoO_2	$\text{Li}_4\text{Ti}_5\text{O}_{12}$	Li(PTFSI) _{0.6} (TFSI) _{0.4} ·1.15H ₂ O	2.4	≈ 100 (at 0.036 A/g)	77% after 100 cycles	[6a]
LiMn_2O_4	Hollow MoS_3 nanospheres	LiTFSI (21 m)	1.35	127 (at 0.1 A/g) 65.1 (at 1 A/g)	70% after 1000 cycles 94% after 1000 cycles	This work

[a] Recalculated based on the mass of the anode materials based on the reference papers.

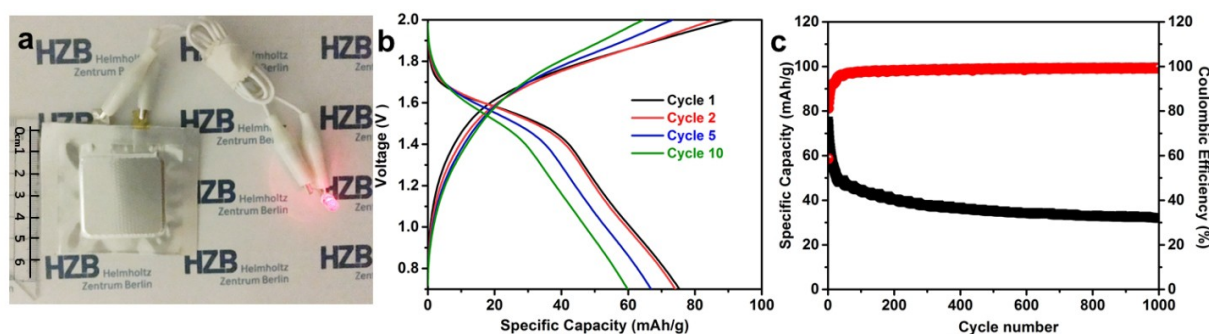


Figure 5. Electrochemical performance of the WISE-based $\text{LiMn}_2\text{O}_4/\text{MoS}_3$ pouch cell. a) Photograph of a pouch cell, b) galvanostatic charge-discharge profiles and c) the cycle life and Coulombic efficiency at 0.1 A/g of the pouch cell.

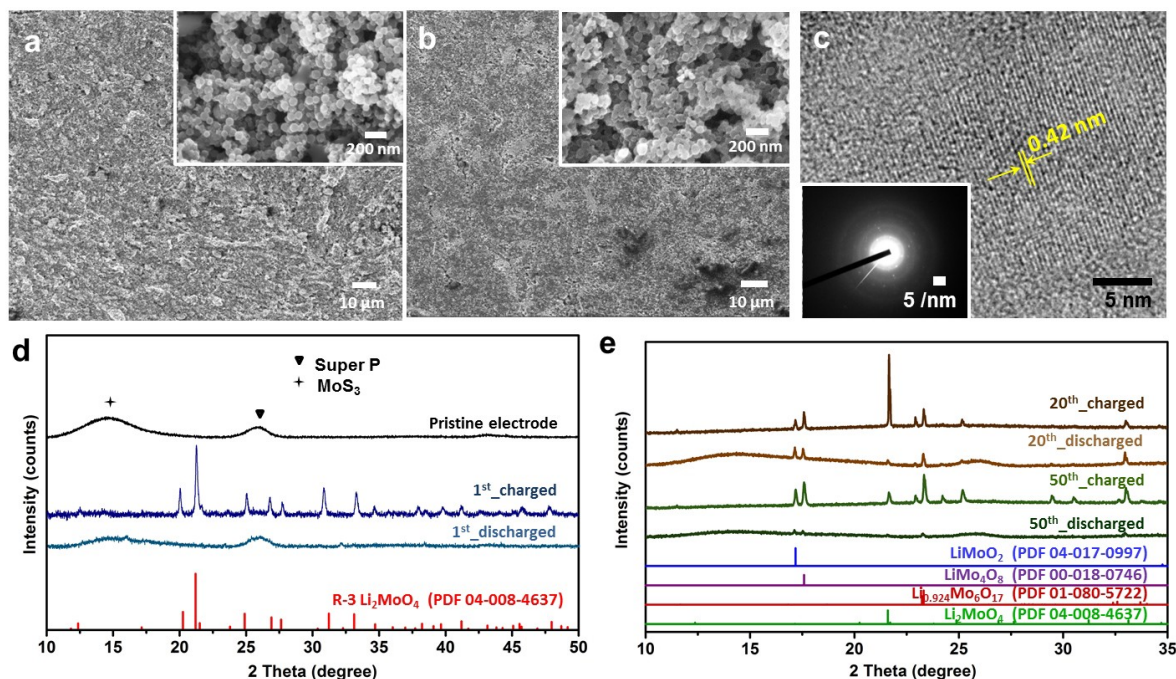


Figure 6. Post-mortem characterization on cycled MoS_3 electrodes. a-b) SEM images of the pristine electrode and the electrode after 400 cycles, respectively, c) HR-TEM image (inset: SAED pattern) of MoS_3 after initial charging, d) XRD patterns of the pristine, 1st_charged and 1st_discharged electrode of MoS_3 & carbon black, e) XRD patterns of the 20th_charged, 20th_discharged, 50th_charged and 50th_discharged electrode of MoS_3 & carbon black. All intensities are absolute.

depressed semicircle corresponding to the charge transfer resistance (R_{ct}) associated with the Li ion transport at the electrode-electrolyte interface, and a slope line in the low frequency range related to the Warburg resistance which reveals the solid diffusion rate of Li ions in the electrode material.^[35] In this work, after different cycles there is no obvious change in R_{br} , indicating the stable electronic conductivity and structure of the electrode over cycling. With the increasing cycles, R_{ct} gradually decreases, revealing the increasingly facilitated Li ion diffusion into the active material during the initial 10 cycles. In addition, after 10 cycles, the EIS spectra see an emerging depressed semicircle at the high frequency region, which represents the presence of an SEI film.^[36] The SEI film protects the electrode material from further parasitic reactions along cycling. The chemical content of the SEI layer may be a LiF-based composite, originating from LiTFSI reduction.^[5]

In order to elucidate the working mechanism of MoS_3 in the WIS-LIBs, XRD measurement was performed on cycled electrodes. In the XRD pattern (Figure 6(d)) of pristine MoS_3 & carbon black (without a binder) pellet electrode, a broad hump at 14° can be observed, arising from the amorphous MoS_3 . The weak and broad bump at 26° is assigned to the carbon black conducting additive in the electrode.^[36] The MoS_3 electrodes were charged and discharged at 20 mA/g to various charge/discharge states and analyzed with XRD.

After initial charging, there appear several new and sharp peaks in the XRD pattern (Figure 6(d)) while the hump of MoS_3 vanishes, indicating the reaction of MoS_3 with the formation of new phase(s), which is identified as R-3 structure rhombohedral

Li_2MoO_4 (PDF #04-008-4637). This is also consistent with high-resolution TEM and SAED in Figure 6(c). The crystalline lattice with a d-space of 0.42 nm in the TEM image can be assigned to the (211) plane of Li_2MoO_4 .^[37] Moreover, it is noted that elemental sulfur is absent in the charged electrode, as seen from the separator extracted from the charged battery, which remains white and clean (Figure S7). After discharging, the sharp crystalline peaks disappear and the hump at 14° and 26° appears again. After 20 and 50 cycles, Li_2MoO_4 remains visible in the XRD peaks (Figure 6(e)) of the charged electrodes but its relative intensity gets weaker and weaker along cycling. Meanwhile, new crystalline peaks emerge in the XRD patterns of charged electrodes, which can be allocated to LiMoO_2 (PDF #04-017-0997), LiMo_4O_8 (PDF #00-018-0746) and $\text{Li}_{0.924}\text{Mo}_6\text{O}_{17}$ (PDF #01-080-5722), as shown in Figure 6(e). The XRD peaks at 23° (in all XRD patterns after 20 and 50 cycles), 29.45° and 30.5° (in the charged electrode after 50 cycles) are yet identified. Moreover, similar to the first cycle, the crystalline peaks of discharged electrodes after 20 and 50 cycles greatly reduce in intensity while the broad humps at 14° and 26° reappear.

Based on these results, it is concluded that amorphous MoS_3 is converted to Li_2MoO_4 together with the evolution of H_2S ($\alpha\text{-MoS}_3 + 2\text{Li}^+ + 2\text{OH}^- + 2\text{H}_2\text{O} \rightarrow \text{Li}_2\text{MoO}_4 + 3\text{H}_2\text{S}\uparrow$) during the initial charging process of the WIS-LIBs. For charge balance, this reaction is accompanied with HER ($2\text{H}^+ + 2\text{e}^- \rightarrow \text{H}_2\uparrow$). After discharging, considering that the conversion from MoS_3 to Li_2MoO_4 (with H_2S evolution, which is indeed a drawback that cannot be neglected and out of study in this work) is apparently irreversible, the delithiated phase(s) upon discharge is identified as amorphous Li-deficient $\text{Li}_{2-x}\text{MoO}_4$ or MoO_x , but

the exact chemical composition is yet known. Along cycling, the repetitive de-/lithiation reaction results in the formation of crystalline Li_xMoO_y phase at charged state and amorphous $\text{Li}_{x-m}\text{MoO}_y/\text{MoO}_2$ upon discharge. Moreover, degradation happens to Li_xMoO_y along cycling, and the ratio of O to Mo in Li_xMoO_y gradually reduces from 4:1 to 3:1 and 2:1. The oxygen-less phases appear to be more stable and reversible during dis-/charge judging from the increasingly improved Coulombic efficiency over cycling. The overall electrochemical process is illustrated in Figure S9.

Compared with the performance of MoS_3 in organic electrolytes based LIBs,^[15a,22,38] the MoS_3 based WIS-LIBs exhibit enhanced cycling stability and rate capability due to the high ionic conductivity of the aqueous electrolyte, and achieve improved manufacturing convenience and environmental benignity. However, the achieved capacity of MoS_3 in the WIS-LIBs is lower than that in organic electrolytes, due to its different reaction mechanism. Moreover, gas evolution happens during the initial cycle(s). This is undesired and hazardous for battery operation, and therefore must be suppressed.

It should be noted that in the MoS_3 based aqueous LIBs, HER, which is supposed to be absent considering the wide electrochemical stability window of the WISE, still occurs. This fact may be attributed to the catalytic behavior of MoS_3 in promoting HER in water splitting systems.^[28,39] The detailed catalytic mechanism of MoS_3 in HER in the WIS-LIBs is out of the scope of the present work. The HER process is undesired and increases the safety concerns during battery charging. Therefore, it is of significant relevance to suppress the HER process, e.g., by reducing the charging cutoff-voltage. We measured the CVs of the WIS-LIBs with decreasing upper voltage limit stepwise from 2.0 V to 1.6 V (Figure S10). It shows that the characteristic HER-associated cathodic profile and the corresponding anodic peak at ~ 1.5 V remain distinct in the CV plots when the upper voltage limit is set to 1.9 V and 1.8 V. Such characteristics vanish when the voltage is limited to ≤ 1.7 V. However, it shows a typical capacitive storage curve and the current response is considerably lower. No peaks are observed in the XRD pattern of the MoS_3 electrode when the battery is charged to 1.6 V (inset of Figure S10(f)), consistent with its capacitive charge storage mechanism. Notably, the achieved capacity charge to 1.6 V is extremely low (8.4 mAh/g at the first cycle), which is far below that of 2 V (127 mAh/g). Thus, the HER process can be suppressed by lowering the charging cutoff voltage, but the achieved capacity would be greatly sacrificed. To avoid gas evolution in practical applications, electrochemical pre-lithiation of MoS_3 (with the conversion to Li_xMoO_y) or exploitation of H_2S adsorbent based electrolyte additive should be considered, but is out of the scope of this work.

The irreversible conversion of MoS_3 to Li_xMoO_y during battery operation stimulates us to study the behaviors of Li ion insertion in MoO_2 . In this work, we compared the performance of MoS_3 and MoO_3 (both in bulk), among which MoO_3 was synthesized by annealing MoS_3 in air, as anode material in the WIS-LIBs. In the CV curves of MoO_3 based WIS-LIBs (Figure S5 (d)), there appears a pair of humps in the initial cycle, which are

assigned to the insertion/desertion of Li ions in the material. With continuous scanning, the two humps become increasingly weaker, indicating the poor irreversibility. The initial specific capacity of bulk MoO_3 is merely 62.1 mAh/g (Figure S5(e)), which is much lower than that of bulk MoS_3 (116 mAh/g, Figure S5(b)). Moreover, MoO_3 presents a rapid capacity fading in the following cycles, showing a worse cycling stability than MoS_3 . The superior performance of MoS_3 can be attributed to its one dimensional chained structure facilitating active Li^+ ion storage during the electrochemical reaction. Moreover, MoO_3 suffers from the dissolution of Mo ions in aqueous electrolytes, which leads to the loss of active materials and thus low capacity retention over cycling.^[40]

3. Conclusions

This work reports a scalable synthesis of hollow MoS_3 nanospheres via an acid-induced precipitation method using removable spherical polyelectrolyte brushes as the template. We have also, for the first time, assessed the capability of MoS_3 as electrode material in aqueous LIBs. When applied in the WIS-LIBs, the hollow nanostructured MoS_3 has achieved promising electrochemical performance with a considerable specific capacity (127 mAh/g) and excellent cycling stability over 1000 cycles. During battery operation, MoS_3 is converted to Li_2MoO_4 in the initial Li^+ ion uptake, and then gradually to a more stable and reversible Li_xMoO_y phase along cycling. The discharge product appears to be amorphous Li-deficient $\text{Li}_{x-m}\text{MoO}_y/\text{MoO}_2$. However, the gas evolution in the initial cycles imposes safety concerns and is to be addressed for practical applications. This work will break new ground for the preparation of metal sulfides/oxides with controlled nanostructures using template based methods and push forward the development of metal sulfides in aqueous energy storage as well as conversion systems.

Experimental Section

Chemicals and materials

Cetyltrimethylammonium bromide (CTAB, Sigma-Aldrich, 99%), 2-Amino-ethylmethacrylate hydrochloride (AEMH, Polyscience, 90%), 2,2'-azobis(2-amidinopropane)dihydrochloride (V50, Sigma-Aldrich, 98%), ammonium tetrathiomolybdate ($(\text{NH}_4)_2\text{MoS}_4$, Sigma-Aldrich), HCl (1 mol/L, Sigma-Aldrich), tetrahydrofuran (THF, Sigma-Aldrich), Poly(tetrafluoroethylene) (PTFE, 60 wt% dispersion in H_2O , Sigma-Aldrich), lithium manganese oxide (LiMn_2O_4 , MTI Corporation), carbon black (super P, Alfa Aesar), water (HPLC grade, Sigma-Aldrich) and LiTFSI (Sigma-Aldrich) were used as received. Styrene (BASF, 99%) was destabilized by Al_2O_3 column and stored in a refrigerator before use. 2-[p-(2-Hydroxy-2-methylpropionophenone)]-ethylene glycol methacrylate (HMEM) was used as the photo-initiator to graft the brushes on the polystyrene (PS) cores.

Synthesis of spherical polyelectrolyte brushes (SPB)

SPB with cationic poly(2-amino-ethylmethacrylate hydrochloride) (PAEMH) brushes was synthesized in a two-step polymerization similar to our previous work.^[41] Polystyrene (PS) was first prepared with a thin layer of HMEM photo-initiator on the surface by emulsion polymerization.^[42] Then the suspension was cleaned through ultrafiltration until the conductivity of the serum reached 20–30 $\mu\text{S}/\text{cm}$. AEMH was chosen as the electrolyte monomer and the polyelectrolyte chains were grafted onto the PS cores by photo-emulsion polymerization. In a typical run, 6.3 g AEMH was slowly added into 650 ml PS-HMEM solution (2.0 wt%), followed by the removal of O_2 through purging with N_2 . UV irradiation was then applied for photo-emulsion polymerization using a UV-reactor (Heraeus TQ150 Z3, range of wavelength 200–600 nm) at room temperature for 60 min. After that, the SPB particles were cleaned by ultrafiltration till the conductivity of the filtrate was between 3 $\mu\text{S}/\text{cm}$ and 5 $\mu\text{S}/\text{cm}$.

Synthesis of hollow MoS_3 nanospheres

The synthesis of hollow MoS_3 nanospheres was achieved with an acid precipitation of MoS_3 on SPB nanospheres followed by removal of the SPB templates. In a typical run, 0.2 g SPB was dispersed in 200 ml water. 0.2 g $(\text{NH}_4)_2\text{MoS}_4$ was added into the SPB solution under stirring. The solution was further stirred for 3 h in order to allow the complete adsorption of MoS_4^{2-} ions onto the surface of the brushes. Next, 1 mol/L HCl was added drop by drop under stirring until the pH of the solution was below 3. The solution was then stirred for another 2 h. During this process, $(\text{NH}_4)_2\text{MoS}_4$ was transformed to MoS_3 accompanied with the evolution of H_2S . The obtained product was collected by centrifugation and was then washed with water for several times. After freeze-drying, it was annealed under argon at 200 °C for 2 h. Finally, the product was obtained after washing with THF and water for several times to remove the SPB templates.

Characterization

Transmission electron microscopy (TEM) and cryogenic transmission electron microscopy (cryo-TEM) images were obtained using a JEOL JEM-2100 instrument operating at an acceleration voltage of 200 kV. X-ray diffraction (XRD) was conducted on a Bruker D8 diffractometer with $\text{Cu K}\alpha$ radiation working at 40 kV. Raman spectroscopy was performed by using a LabRAM HR Evolution Raman spectrometer with a HeNe laser as the excitation line at λ (wavelength) = 633 nm. X-ray photoelectron spectroscopy (XPS) measurements were carried out on an ESCALAB 250Xi spectrometer (ThermoFisher Scientific). For the XRD measurement on cycled electrodes, pellet-like electrodes composed of hollow MoS_3 nanospheres-carbon black (8:2 in mass) excluding binder were utilized. The electrodes were extracted from charged/discharged batteries and dried at natural conditions prior to the XRD measurements. Scanning electron microscopy (SEM) on the pristine and cycled electrodes was carried out on a SEM LEO GEMINI 1530 microscope equipped with an energy-dispersed X-ray (EDS) detector (Thermo Fischer) and the cycled electrode was cleaned thoroughly with water and dried before imaging. Scanning transmission electron microscopy (STEM) was performed on a JEOL JEM-2200F5 transmission electron microscope operated at 200 kV and equipped with a high-angle annular dark-field (HAADF) STEM detector and a Bruker silicon drift detector for EDS. N_2 adsorption/desorption isotherms were obtained using a Quantachrome Autosorb-1 system at 77 K. The specific surface area was calculated using the Brunauer-Emmett-Teller (BET) method based on a multi-point analysis.

Electrochemical Measurements

The electrochemical properties of MoS_3 hollow nanospheres based WIS-LIBs were evaluated in three-electrode configuration, CR 2032 type coin cells as well as pouch cells testing. Three-electrode configuration was conducted using MoS_3 ($\sim 40 \mu\text{g}$) on glassy carbon (0.077 cm^2) as working electrode, Ag/AgCl as reference electrode and platinum wire as counter electrode. In coin cells and pouch cells, a WISE of 21 m LiTFSI dissolved in water (21 mol LiTFSI in 1 kg water) was used as the working electrolyte and a glass fiber (Whatman) was used as the separator. The electrodes were fabricated by uniformly mixing and compressing LiMn_2O_4 , carbon black and PTFE (weight ratio of 8:1:1) for cathodes and hollow MoS_3 nanospheres, carbon black and PTFE (weight ratio of 7:2:1) for anodes between two pieces of stainless steel (SS, type 316, 40 mesh) grids, respectively. The SS grids were thoroughly cleaned with ethanol under ultrasonication, followed by washing with deionized water and drying before use. The mass ratio of cathode/anode materials was set to 2:1 and the mass loading of MoS_3 was about 2 mg/cm^2 . The pouch cells were assembled with a MoS_3 electrode as anode and a LiMn_2O_4 electrode as cathode. A 15 μm thick Ti tab was used as the current collector for both electrodes. Excess amount of electrolyte ($\sim 100 \mu\text{L}/\text{cm}^2$) was used and the cells were sealed with a vacuum sealer. No external pressure was applied on the pouch cells during electrochemical cycling. Galvanostatic electrochemical cycling and cyclic voltammetry (CV) were carried out between 0.7 V and 2.0 V with a Biologic electrochemical workstation (MPG2 galvanostatic/potentiostat). All calculations of the specific capacity are based on the mass of anode materials. All batteries were tested directly without any activation procedures.

Acknowledgements

T.Q. gratefully acknowledges financial support of CSC scholarship. Y.L.X. acknowledges the Humboldt Fellowship for Postdoctoral Researchers from the Alexander von Humboldt Foundation for financial support. The authors also thank the Joint Lab for Structural Research at the Integrative Research Institute for the Sciences (IRIS Adlershof).

Conflict of Interest

The authors declare no conflict of interest.

Keywords: MoS_3 · hollow nanostructure · “water-in-salt” electrolyte (WISE) · Li-ion batteries

- [1] a) J. B. Goodenough, K. S. Park, *J. Am. Chem. Soc.* **2013**, *135*, 1167–1176; b) M. S. Whittingham, *Chem. Rev.* **2004**, *104*, 4271–4301; c) Y. S. Huang, D. Q. Wu, J. Z. Jiang, Y. Y. Mai, F. Zhang, H. Pan, X. L. Feng, *Nano Energy* **2015**, *12*, 287–295.
- [2] a) M. Armand, J. M. Tarascon, *Nature* **2008**, *451*, 652–657; b) K. Xu, *Chem. Rev.* **2004**, *104*, 4303–4417; c) J. F. Parker, C. N. Chervin, I. R. Pala, M. Machler, M. F. Burz, J. W. Long, D. R. Rolison, *Science* **2017**, *356*, 414–417.
- [3] a) L. Xue, Q. H. Zhang, X. H. Zhu, L. Gu, J. L. Yue, Q. Y. Xia, T. Xing, T. T. Chen, Y. Yao, H. Xia, *Nano Energy* **2019**, *56*, 463–472; b) H. Glatz, E. Tervoort, D. Kundu, *ACS Appl. Mater. Interfaces* **2020**, *12*, 3522–3530.

- [4] a) H. Kim, J. Hong, K. Y. Park, H. Kim, S. W. Kim, K. Kang, *Chem. Rev.* **2014**, *114*, 11788–11827; b) Y. G. Wang, J. Yi, Y. Y. Xia, *Adv. Energy Mater.* **2012**, *2*, 830–840; c) W. Li, J. R. Dahn, D. S. Wainwright, *Science* **1994**, *264*, 1115–1118.
- [5] L. M. Suo, O. Borodin, T. Gao, M. Olguin, J. Ho, X. L. Fan, C. Luo, C. S. Wang, K. Xu, *Science* **2015**, *350*, 938–943.
- [6] a) S. Ko, Y. Yamada, K. Miyazaki, T. Shimada, E. Watanabe, Y. Tateyama, T. Kamiya, T. Honda, J. Akikusa, A. Yamada, *Electrochem. Commun.* **2019**, *104*, 5; b) L. M. Suo, O. Borodin, W. Sun, X. L. Fan, C. Y. Yang, F. Wang, T. Gao, Z. H. Ma, M. Schroeder, A. von Cresce, S. M. Russell, M. Armand, A. Angell, K. Xu, C. S. Wang, *Angew. Chem. Int. Ed.* **2016**, *55*, 7136–7141; *Angew. Chem.* **2016**, *128*, 7252–7257.
- [7] a) Y. Yamada, K. Usui, K. Sodeyama, S. Ko, Y. Tateyama, A. Yamada, *Nat. Energy* **2016**, *1*, 9; b) N. Dubouis, P. Lemaire, B. Mirvaux, E. Salager, M. Deschamps, A. Grimaud, *Energy Environ. Sci.* **2018**, *11*, 3491–3499.
- [8] a) D. Reber, R. S. Kuhnle, C. Battaglia, *Sustain. Energ. Fuels* **2017**, *1*, 2155–2161; b) S. Ko, Y. Yamada, A. Yamada, *ACS Appl. Mater. Interfaces* **2019**, *11*, 45554–45560.
- [9] L. M. Suo, D. Oh, Y. X. Lin, Z. Q. Zhuo, O. Borodin, T. Gao, F. Wang, A. Kushima, Z. Q. Wang, H. C. Kim, Y. Qi, W. L. Yang, F. Pan, J. Li, K. Xu, C. S. Wang, *J. Am. Chem. Soc.* **2017**, *139*, 18670–18680.
- [10] a) M. R. Lukatskaya, J. I. Feldblyum, D. G. Mackanic, F. Lissel, D. L. Michels, Y. Cui, Z. A. Bao, *Energy Environ. Sci.* **2018**, *11*, 2876–2883; b) J. Lim, K. Park, H. Lee, J. Kim, K. Kwak, M. Cho, *J. Am. Chem. Soc.* **2018**, *140*, 15661–15667.
- [11] a) L. N. Qu, X. H. Hou, X. Y. Huang, Q. Liang, Q. Ru, B. Wu, K. H. Lam, *ChemElectroChem* **2017**, *4*, 3148–3155; b) D. E. Demirocak, S. S. Srinivasan, E. K. Stefanakos, *Appl. Sci.-Basel* **2017**, *7*, 26.
- [12] a) Y. Wang, J. J. Wu, Y. F. Tang, X. J. Li, C. Y. Yang, M. S. Qin, F. Q. Huang, X. Li, X. Zhang, *ACS Appl. Mater. Interfaces* **2012**, *4*, 4246–4250; b) C. Xu, Y. Zeng, X. H. Rui, N. Xiao, J. X. Zhu, W. Y. Zhang, J. Chen, W. L. Liu, H. T. Tan, H. H. Hng, Q. Y. Yan, *ACS Nano* **2012**, *6*, 4713–4721; c) L. Zhang, H. B. Wu, Y. Yan, X. Wang, X. W. Lou, *Energy Environ. Sci.* **2014**, *7*, 3302–3306.
- [13] J. G. Wang, H. Y. Liu, R. Zhou, X. R. Liu, B. Q. Wei, *J. Power Sources* **2019**, *413*, 327–333.
- [14] a) Y. M. Shi, W. Zhou, A. Y. Lu, W. J. Fang, Y. H. Lee, A. L. Hsu, S. M. Kim, K. K. Kim, H. Y. Yang, L. J. Li, J. C. Idrobo, J. Kong, *Nano Lett.* **2012**, *12*, 2784–2791; b) Y. Q. Teng, H. L. Zhao, Z. J. Zhang, Z. L. Li, Q. Xia, Y. Zhang, L. N. Zhao, X. F. Du, Z. H. Du, P. P. Lv, K. Swierczek, *ACS Nano* **2016**, *10*, 8526–8535.
- [15] a) U. Chang, J. T. Lee, J. M. Yun, B. Lee, S. W. Lee, H. I. Joh, K. Eom, T. F. Fuller, *ACS Nano* **2019**, *13*, 1490–1498; b) J. F. Sun, R. T. Wang, C. Z. Yuan, *Mater. Today* **2018**, *21*, 193–194; c) Z. P. Huang, C. F. Wang, L. Pan, F. Tian, X. X. Zhang, C. Zhang, *Nano Energy* **2013**, *2*, 1337–1346.
- [16] A. J. Jacobson, R. R. Chianelli, S. M. Rich, M. S. Whittingham, *Mater. Res. Bull.* **1979**, *14*, 1437–1448.
- [17] J. C. Wildervanck, F. Jellinek, Z. Anorg. Allg. Chem. **1964**, *328*, 309–318.
- [18] J. Wang, S. H. Ng, S. Y. Chew, D. Wexler, G. X. Wang, H. K. Liu, *Electrochem. Solid-State Lett.* **2007**, *10*, A204–A207.
- [19] T. Zhang, L. B. Kong, Y. H. Dai, K. Yan, M. Shi, M. C. Liu, Y. C. Luo, L. Kang, *Chem. Asian J.* **2016**, *11*, 2392–2398.
- [20] J. J. Auborn, Y. L. Barberio, K. J. Hanson, D. M. Schleich, M. J. Martin, *J. Electrochem. Soc.* **1987**, *134*, 580–586.
- [21] Y. L. Zhou, Y. Y. Li, Q. Q. Wang, Q. Wang, R. Du, M. Zhang, X. Q. Sun, X. Y. Zhang, L. T. Kang, F. Y. Jiang, *ChemElectroChem* **2019**, *6*, 3113–3119.
- [22] X. D. Li, G. X. Wu, J. W. Chen, M. C. Li, W. Li, T. Y. Wang, B. Jiang, Y. He, L. Q. Mai, *Appl. Surf. Sci.* **2017**, *392*, 297–304.
- [23] H. L. Ye, L. Wang, S. Deng, X. Q. Zeng, K. Q. Nie, P. N. Duchesne, B. Wang, S. Liu, J. H. Zhou, F. P. Zhao, N. Han, P. Zhang, J. Zhong, X. H. Sun, Y. Y. Li, Y. G. Li, J. Lu, *Adv. Energy Mater.* **2017**, *7*, 9.
- [24] H. Wei, S. X. Cheng, X. Z. Zhang, R. X. Zhuo, *Prog. Polym. Sci.* **2009**, *34*, 893–910.
- [25] a) Z. M. Zheng, P. Li, J. S. Huang, H. D. Liu, Y. Zao, Z. L. Hu, L. Zhang, H. X. Chen, M. S. Wang, D. L. Peng, Q. B. Zhang, *J. Energy Chem.* **2020**, *41*, 126–134; b) H. Q. Liu, K. Z. Cao, W. Y. Li, Q. Q. Han, R. T. Zheng, J. Shu, Z. Zhang, K. J. Huang, Q. S. Jing, L. F. Jiao, *J. Power Sources* **2019**, *437*, 8; c) B. Q. Li, S. Y. Zhang, L. Kong, H. J. Peng, Q. Zhang, *Adv. Mater.* **2018**, *30*, 6.
- [26] a) Y. Mei, Y. Lu, F. Polzer, M. Ballauff, M. Drechsler, *Chem. Mater.* **2007**, *19*, 1062–1069; b) S. Gu, Y. Lu, J. Kaiser, M. Albrecht, M. Ballauff, *Phys. Chem. Chem. Phys.* **2015**, *17*, 28137–28143.
- [27] C. Sourisseau, O. Gorochov, D. M. Schleich, *Mater. Sci. Eng. B* **1989**, *3*, 113–117.
- [28] H. Vrubel, D. Merki, X. L. Hu, *Energy Environ. Sci.* **2012**, *5*, 6136–6144.
- [29] H. L. Ye, L. Ma, Y. Zhou, L. Wang, N. Han, F. P. Zhao, J. Deng, T. P. Wu, Y. G. Li, J. Lu, *Proc. Natl. Acad. Sci. USA* **2017**, *114*, 13091–13096.
- [30] T. Gao, X. Ji, S. Hou, X. L. Fan, X. G. Li, C. Y. Yang, F. D. Han, F. Wang, J. J. Jiang, K. Xu, C. S. Wang, *Adv. Mater.* **2018**, *30*, 8.
- [31] L. M. Suo, F. D. Han, X. L. Fan, H. L. Liu, K. Xu, C. S. Wang, *J. Mater. Chem. A* **2016**, *4*, 6639–6644.
- [32] L. M. Suo, O. Borodin, Y. S. Wang, X. H. Rong, W. Sun, X. L. Fan, S. Y. Xu, M. A. Schroeder, A. V. Cresce, F. Wang, C. Y. Yang, Y. S. Hu, K. Xu, C. S. Wang, *Adv. Energy Mater.* **2017**, *7*, 10.
- [33] P. C. Shi, H. Zheng, X. Liang, Y. Sun, S. Cheng, C. H. Chen, H. F. Xiang, *Chem. Commun.* **2018**, *54*, 4453–4456.
- [34] J. Cannarella, C. B. Arnold, *J. Power Sources* **2014**, *245*, 745–751.
- [35] L. L. Perreault, F. Colo, G. Meligrana, K. Kim, S. Fiorilli, F. Bella, J. R. Nair, C. Vitale-Brovarone, J. Florek, F. Kleitz, C. Gerbaldi, *Adv. Energy Mater.* **2018**, *8*, 12.
- [36] M. Marinaro, M. Mancini, F. Nobili, R. Tossici, L. Damen, R. Marassi, *J. Power Sources* **2013**, *222*, 66–71.
- [37] X. D. Liu, Y. C. Lyu, Z. H. Zhang, H. Li, Y. S. Hu, Z. X. Wang, Y. M. Zhao, Q. Kuang, Y. Z. Dong, Z. Y. Liang, Q. H. Fan, L. Q. Chen, *Nanoscale* **2014**, *6*, 13660–13667.
- [38] T. Matsuyama, A. Hayashi, T. Ozaki, S. Mori, M. Tatsumisago, *J. Mater. Chem. A* **2015**, *3*, 14142–14147.
- [39] T. Bourgeteau, D. Tondelier, B. Geffroy, R. Brisse, C. Laberty-Robert, S. Campidelli, R. de Bettignies, V. Artero, S. Palacin, B. Josselme, *Energy Environ. Sci.* **2013**, *6*, 2706–2713.
- [40] W. Tang, L. L. Liu, Y. S. Zhu, H. Sun, Y. P. Wu, K. Zhu, *Energy Environ. Sci.* **2012**, *5*, 6909–6913.
- [41] M. Yu, Y. Lu, M. Schrunner, E. Polzer, M. Ballauff, *Macromol. Symp.* **2007**, *254*, 42–45.
- [42] M. Ballauff, *Prog. Polym. Sci.* **2007**, *32*, 1135–1151.

Manuscript received: February 26, 2020

Revised manuscript received: March 26, 2020

Accepted manuscript online: April 8, 2020

Version of record online: April 27, 2020